OPTICA

Laboratory soft X-ray setup for transient absorption experiments in the liquid phase using a laser-produced plasma source

Richard Gnewkow,[1,2,3,*] Holger Stiel,[3,4] Adrian Jonas,[5] Silvana Schönfelder,[2,3,6] Jürgen Probst,[7] Thomas Krist,[7] Birgit Kanngiesser,[1,2,3] and Ioanna Mantouvalou[1,2,3]

[1]Helmholtz Zentrum Berlin, 12489 Berlin, Germany
[2]Technische Universität Berlin, Institut für Optik und Atomare Physik, 10623 Berlin, Germany
[3]Berlin Laboratory for innovative X-ray technologies (BLiX), 10623 Berlin, Germany
[4]Max-Born-Institut für Nichtlineare Optik und Kurzzeitspektroskopie, 12489 Berlin, Germany
[5]Physikalisch-Technische Bundesanstalt, 10587 Berlin, Germany
[6]Current address: Universität Greifswald, Institut für Physik, 17489 Greifswald, Germany
[7]NOB Nano Optics Berlin GmbH, 10627 Berlin, Germany
*richard.gnewkow@helmholtz-berlin.de

Received 9 January 2024; revised 18 March 2024; accepted 7 April 2024; published 22 May 2024

With time-resolved soft X-ray spectroscopy, the element-specific dynamics of the electronic structure of disordered systems can be investigated. Measurements of species in dilute liquid solutions are particularly challenging and require high photon flux combined with low experimental noise. This mostly limited these experiments to large-scale facilities, especially for energies above the water window (533 eV). Based on a laser-produced plasma source, our system enables, to the best of our knowledge, the first static and transient experiments in the liquid phase to be performed in the laboratory for energies up to 1400 eV and with a time resolution of 500 ps. We benchmark the system with static investigations of $[Ni(CN)_4]^{2-}$ and transient experiments on the widely used model complex $[Fe(bpy)_3]^{2+}$, both in an aqueous solution. The introduced self-referencing concept ensures that the measurements are photon noise limited. Our results form the basis for further liquid-phase experiments investigating the dynamics in diluted solutions.

https://doi.org/10.1364/OPTICA.517698

1. INTRODUCTION

Soft X-ray absorption spectroscopy, also called near-edge X-ray absorption fine structure (NEXAFS) spectroscopy, is an established tool to study the electronic and structural properties of molecules and catalysts [1,2]. Because core-level transitions are measured, the method is element-specific and sensitive to the local environment. When using soft X-rays, NEXAFS spectroscopy directly probes the valence orbitals of the 3D transition metals and gives access to light elements such as carbon, nitrogen, and oxygen. Performing NEXAFS experiments in the liquid phase is particularly interesting because the behavior of materials in solution often dictates their functionality and reactivity [3,4]. However, liquid phase experiments in the soft X-ray regime are not trivial because the absorption of the liquid is typically comparable to the sample's absorption. In combination with low solubility down to the micromolar range for many biological and chemical systems, the signal becomes very small. As a result, these studies are generally carried out at large-scale facilities due to the required high source brightness. Improvements in laser and optics technology in recent years now facilitate these experiments in the laboratory with the benefit of easier access and availability. Possible sources are either based on high harmonic generation (HHG) or laser-produced plasma (LPP) generation. HHG sources have already been applied for liquid phase NEXAFS experiments [5,6], and cutoff energies above 600 eV were demonstrated [7–11]. Still, HHG remains challenging for higher energies because the required long-wavelength driving lasers need a high average power to compensate for the reduced conversion efficiency. In comparison, LPP sources offer a high photon flux even at 1400 eV [12] with lower laser requirements but also with lower temporal resolution.

The first part of this work describes the developed setup for transmission mode NEXAFS in the liquid phase based on a broadband LPP source. Performing the measurements in transmission mode is the most efficient method when using a broadband source. It provides access to the absolute absorption cross-section and avoids self-absorption effects, unlike fluorescence or electron yield detection schemes. However, in-vacuum operation and a suitable sample delivery system are necessary because nanometer to few micrometers thin liquid films are needed for an optimal absorption edge jump. This problem is solved either by transmission liquid cells [13–24] or by using flatjets [25–31], which form a thin flat sheet. Such free-flowing jets have the advantage of no additional

absorption caused by windows, and the sample is replenished after every X-ray shot. Our setup uses the widely used flatjet option with two separate nozzles [32].

The LPP source delivers intense, isotropic, pulsed, and broadband soft X-rays from 100–1400 eV, covering most L and M edges of the transition metal and rare earth elements. Combined with a spectrometer that uses novel reflection zone plates (RZP) on spherical substrates, this setup detects two orders of magnitude more photons than other laboratory setups that can perform liquid phase experiments. Additionally, the introduction of a new detection scheme that takes advantage of the highly divergent source emission results in photon noise-limited detection. The LPP setup allows for time-resolved investigations in addition to static measurements. This is achieved by optical excitation of the sample with part of the driving laser before the sample is probed with the X-ray pulse. By changing the time delay between the two pulses, the temporal dynamics of short-lived states can be investigated. This pump-probe scheme allows tracking of chemical and geometric changes with element specificity and sub-nanosecond time resolution.

In the second part, the potential of the developed setup with high detected photon numbers and low experimental noise is demonstrated on two prototypical samples: $[Ni(CN)_4]^{2-}$ for static experiments and $[Fe(bpy)_3]^{2+}$ for time-resolved measurements. Metal cyanide compounds in aqueous solutions, especially the iron-containing $K_4Fe(CN)_6$, were already studied in numerous publications as model complexes to test fundamental concepts of metal coordination and metal-to-ligand charge transfer (MLCT) processes [33,34]. In this context, we present the first liquid phase measurements of $[Ni(CN)_4]^{2-}$ with results for all three elemental components. At the nitrogen K-edge of $[Fe(bpy)_3]^{2+}$, we demonstrate the time-resolved capabilities of the setup on a popular model system for intersystem crossing after photoexcitation [35] and compare the results to synchrotron measurements. The first time-resolved measurement of $[Fe(bpy)_3]^{2+}$ at the carbon K-edge, together with quantum chemical calculations, reveals that investigations at the carbon K-edge can help answer the ultrafast relaxation pathway.

In the third part, the capabilities of the setup are compared to HHG and synchrotron sources. Additionally, possible improvements to the setup are discussed to facilitate measurements with sub-millimolar concentrations.

2. MATERIALS AND METHODS

In previous publications, we have described our in-house setup for solid-phase samples in detail [36–38]. In our LPP setup, a thin disk laser (1030 nm, < 200 mJ pulse energy, 500 ps pulse duration, 100 Hz repetition rate) is focused onto a rotating metal cylinder. This process creates a plasma that emits isotropic, broadband, and pulsed radiation, covering the soft X-ray region from 100–1400 eV. A tungsten target is used for NEXAFS experiments because of its quasi-continuous X-ray emission. Copper and iron targets are used for their well-characterized, discrete emission lines to calibrate the energy axis [39] without a reference sample. All components are contained in a vacuum chamber with a pressure of 10^{-7} mbar. More information about the setup can be found in Section S1 in Supplement 1.

Here, we present the extension of this setup to liquid-phase experiments. This is facilitated by a flatjet system in combination with a novel RZP on a curved substrate, as described below.

A. Flatjet

The liquid phase transmission experiments are enabled by a commercial flatjet system with a catcher system manufactured by Advanced Microfluidic Systems GmbH. The flatjet creates liquid sheets inside the vacuum chamber by colliding two cylindrical liquid jets [25,40–43] generated by a pair of nozzles with a 33 µm inner diameter under a 45° angle, as shown in Fig. 1(a). A flow rate of 1.9 ml/min and a pressure of 20 bar is used for all measurements. For water, these parameters create a first oval sheet with a width of 0.22 mm and a height of 1.05 mm. The maximum thickness is 3.5 µm. After the end of the first sheet, the liquid is collected by a catcher system that transports the liquid out of the vacuum chamber into a reservoir. This makes continuous recycling down to a volume of 10 ml possible and allows liquid phase experiments on precious sample systems. As an estimate, around 100 µg sample is required for a typical concentration of 30 mM/l.

Flatjet measurements are often performed with aqueous solutions because water easily forms a stable jet. Nevertheless, using a wide range of solvents is desirable to increase the selection of sample systems. By cooling the solvent, high vapor pressure solvents were already successfully used with a flatjet (e.g., acetonitrile with a vapor pressure of 0.12 bar [44]). We performed, to the best of our knowledge, the first flatjet measurement of acetone with an even higher vapor pressure of 0.24 bar at the oxygen K-edge, as shown in Fig. 2(d). In addition to acetone, other organic solvents such

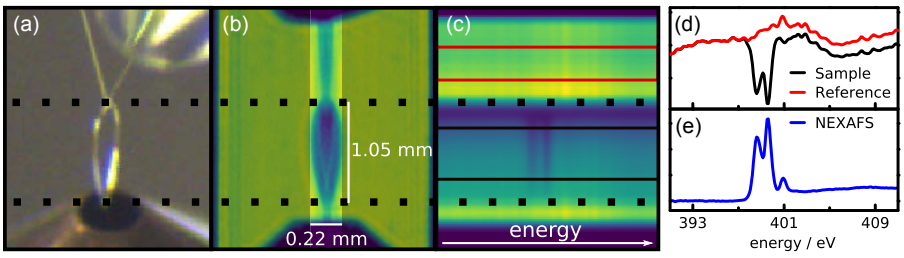

Fig. 1. Dashed black lines in images (a)–(c) mark the start and end of the first liquid leaf. In the top part are the two nozzles and the bottom part is the catcher. (a)–(c) Same running jet. (a) Optical camera image of the running flatjet. (b) The zeroth diffraction order of the RZP on the CCD detector gives a direct image of the nozzles, flatjet, and catcher in the form of an X-ray absorption contrast image. The darkened area indicates the position of the slit to the left and right of the jet. (c) Detector image of the first diffraction order of the RZP. The solid black band marks the region on the flatjet used to generate the N K-edge spectrum of $[Ni(CN)_4]^{2-}$ shown in (d). The mean jet thickness in this region is 2 µm. The solid red band is used to generate the reference spectrum. (d) Spectra obtained after averaging the individual pixel columns in the marked areas. (e) NEXAFS spectrum for the sample and reference spectra from (d) with a measurement time of 20 min and a concentration of 130 mM.

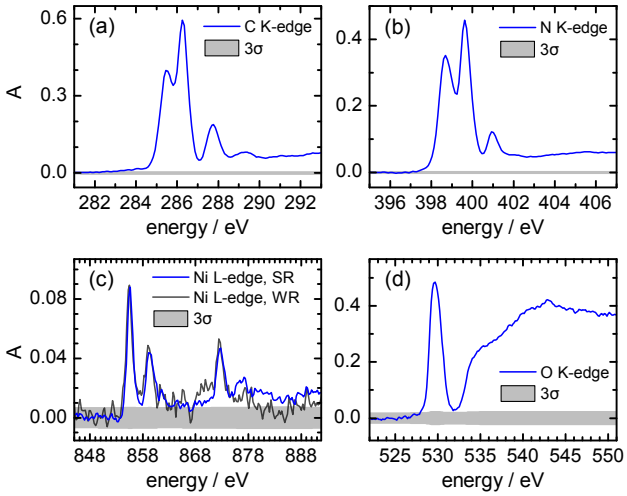

Fig. 2. (a)–(c) $[Ni(CN)_4]^{2-}$ NEXAFS spectra of 130 mM aqueous solution for all three elements together with the 3σ range shown as gray bars around zero. The blue curves are the results obtained with the self-reference method (SR). The black curve in (c) is obtained with a separate reference measurement of a pure water jet (WR). (d) Oxygen K-edge spectrum of acetone with a solvent temperature of 0°C.

as cyclohexanone or 2-pentanone formed a stable jet in vacuum and could be recycled. This demonstrates that modern flatjet systems offer great flexibility regarding solvents in combination with sample recycling. See Section S2 in Supplement 1 for more information about the flatjet.

B. RZP Spectrometer and Data Treatment

The dispersion and focusing of the polychromatic X-ray emission onto the CCD detector is achieved by novel off-axis reflection zone plates (RZP) on a spherical substrate [45,46] manufactured by NOB Nano Optics Berlin GmbH. The RZP collects a few 100 eV bandwidths from the isotropic and polychromatic source and maps the different energies as straight lines onto the detector. Due to the spherical substrate, the energy window with sharp energy focusing is a couple of 100 eV, which enables the simultaneous detection of adjacent absorption edges. The height information in the sample plane is preserved with a resolution around 50 µm FWHM, depending on the energy. The main parameters of the source and RZP are summarized in Table 1. More information can be found in Section S3 in Supplement 1.

Since the RZP viewing area of $1.3 \times 3.2\ mm^2$ (w × h) at the flatjet position is larger than the jet ($0.22 \times 1.05\ mm^2$), the width is restricted with a slit to the maximum jet extend of 0.22 mm, reducing the effective solid angle of detection to 1.1×10^{-7} sr. This can be seen in Fig. 1(b), which shows the zeroth diffraction order of the RZP structure on the detector, corresponding to the total external reflection of the broadband emission of the LPP source. Only the relevant region of the RZP viewing area is shown in the image for better visibility. The resulting absorption contrast gives a two-dimensional image of the complete flatjet system. It is used for a reproducible alignment of the slit, catcher, and nozzles into the beam path.

In the first diffraction order, shown in Fig. 1(c), the horizontal direction is the energy axis with a resolving power of around 1000. In the vertical direction, the RZP has the same height resolution of around 50 µm as in the zeroth order. This makes a height restriction in the sample plane unnecessary because the height resolution of the RZP is used in the data evaluation to select the flatjet region with the best signal-to-noise ratio (SNR), depending on the sample concentration and solvent absorption (S4). The simultaneous measurement of an area extending over the whole flatjet sheet is an important difference compared to synchrotron or HHG measurements, where only a small area in the micrometer range is usually measured.

An advantage of this method is that the region on the detector image between the nozzles and the start of the liquid sheet, marked in red in Fig. 1(c), can be used as a reference spectrum as long as the solvent does not have absorption features at the investigated absorption edges. This self-reference method uses the same RZP structure and diffraction order to detect the complete sample and reference spectra for every X-ray shot, ensuring artifact-free detection. The spectrometer is, therefore, less sensitive against jet or source instabilities, and no separate reference measurement is needed. For the self-reference method, the intensity of the reference spectrum is adjusted in data post-processing to the pre-edge intensity of the sample spectrum with a single exponential function to correct for the additional solvent absorption absent in the reference data (S5).

Similar detection schemes were implemented utilizing different diffraction orders of gratings [47–51] or transmission zone plates [52] at the European XFEL. An advantage of our approach is that no flat-field correction has to be performed since we use the same reflection order for both spectra. As a result, our data are completely photon noise limited down to an absorption of at least 7×10^{-4} A, which will be shown in Section 3 (Results and Discussion). The absorption A and the absorption difference in time-resolved measurements ΔA is defined as

$$A = \ln\left(\frac{I_R}{I_{S_G}}\right), \quad \Delta A = A_E - A = \ln\left(\frac{I_R}{I_{S_E}}\right) - \ln\left(\frac{I_R}{I_{S_G}}\right) = \ln\left(\frac{I_{S_G}}{I_{S_E}}\right), \tag{1}$$

Table 1. Source, Optic, and Spectrometer Performance Values for the Flatjet Measurements[a]

Source		Zone Plates [45]		With Flatjet	
Energy range	100–1400 eV	Energy range	210–1400 eV	Effective solid angle	1.1×10^{-7} sr
Peak brilliance	10^{11} ph/mm^2/mrad^2/s/line [36]	Energy resolving power	1000	Detected photons C K-edge	8×10^3/s/0.1%BW
Peak spectral radiant intensity	10^{13} ph/s/sr/0.1%BW [12]	Solid angle	9×10^{-6} sr	Detected photons N K-edge	3×10^4/s/0.1%BW
X-ray duration	500 ps	Peak reflectivity	25%	Detected photons Ni L-edge	3×10^3/s/0.1%BW

[a]The effective solid angle includes the reflectivity and the reduced solid angle due to the slit in the horizontal direction. The detected photon numbers are the measured values in the sample spectrum for a 130 mM aqueous solution of $[Ni(CN)_4]^{2-}$ shown in Fig. 2.

with the transmitted intensity of the pure solvent I_R, the transmitted intensity through the sample, and the solvent without optical excitation I_{S_G} and with optical excitation I_{S_E}.

C. Sample Preparation

$K_2Ni(CN)_4xH_2O$(II) (415154-100G) was purchased from Sigma-Aldrich. The Ni complex was prepared as a 130 mM solution in deionized water with a volume of 150 ml. $[Fe(bpy)_3]Cl_2$ ($C_{30}H_{24}Cl_2FeN_6$) was purchased from HetCat and prepared as a 30 mM solution in 150 ml of deionized water. Acetone ($\geq$ 99.7%) was purchased from Carl Roth GmbH. All measurements are performed with the catcher and the same recycled sample solutions without additional filtering, purification, or concentration adjustment.

D. Quantum Mechanical Calculations

For spectra analysis, DFT simulations were performed with ORCA 5.0.4. Geometry optimization and TD-DFT calculations are performed with the B3LYP functional and the def2-TZVP basis set. The RIJCOSX method with def2/J as an auxiliary basis set is used. The CPCM emulates the water environment. The NEXAFS spectra are calculated with TD-DFT using the TDA approximation and D3BJ correction. The calculation is repeated for every carbon atom with only the 1 s orbital included in the donor space to obtain the contribution of the single carbon atoms. The N K-edge spectra are convoluted with a Voigt function (0.5 eV Lorentzian, 0.5 Gaussian) and shifted by 12.17 eV to match the measured spectra. The C K-edge spectra are broadened with a Voigt function (0.7 eV Lorentzian, 0.45 Gaussian) and shifted by 10.4 eV. The large broadening is required to account for the vibrational structure of $[Fe(bpy)_3]^{2+}$ [53].

3. RESULTS AND DISCUSSION

A. $Ni(CN)_4$

Figure 2 shows the NEXAFS spectra for all elements in $[Ni(CN)_4]^{2-}$ together with the 3σ interval of the photon shot noise (S7). Measurements at the C K-edge were recorded in 37 min, the N K-edge data was obtained in 20 min, and the Ni L-edge data was obtained in 17 min. The separate reference measurement at the Ni L-edge with pure DI water was recorded in 17 min.

While a large number of publications exists about the iron cyanide complex in the liquid phase [54–57], for the Ni-complex the only published X-ray data is for solid samples at the L-edge [58,59]. Because our Ni L-edge data in solution is in good agreement with the published solid phase measurement and studies of the solvent effects for other cyanide compounds [60,61] showed only a small influence on the spectral shape at the L-edge, we use these earlier publications to identify the transitions.

Due to the strong field CN^- ligands, the Ni(II) d^8 complex will be a low spin with square planar geometry and D_{4h} symmetry. The NEXAFS spectrum at the Ni L-edge consists of two similar absorption structures (L_3 and L_2 edge) caused by the large spin-orbit coupling of the $2p$ core hole. The first peak at 855.6 eV is a transition into the unoccupied metal $3d_{x2-y2}$ orbital and the second peak at 859.3 eV probes the hybridized ligand $2p$-metal 3D orbitals.

Two Ni L-edge NEXAFS spectra are shown for the sample data set to demonstrate the advantage of the self-referencing method. The Ni spectrum shown in blue is obtained with the self-reference method, whereas the Ni spectrum in black is obtained with an additional reference measurement of a pure water jet. The comparison shows that source and jet fluctuations can lead to spectral distortions and noise values outside the 3σ when the sample and the reference spectra are recorded separately. The use of the self-reference method minimizes this influence.

We attribute the transitions for the carbon and nitrogen K-edge NEXAFS from the 1 s orbitals localized at the CN^- ligand into the unoccupied π^* manifold, analog to the Fe-complex interpretations. This results in an almost identical absorption structure concerning the intensity and the energy distance between the different transitions at the carbon and nitrogen edges.

B. $Fe(bpy)_3$

In the following, time-resolved measurements of $[Fe(bpy)_3]^{2+}$ at the N and C K-edge combined with quantum mechanical calculations to interpret the results are presented. For all measurements, a fluence of 120 mJ/cm^2 at 515 nm is used with a beam diameter of 1.8 mm FWHM.

The results for the transient N K-edge $[Fe(bpy)_3]^{2+}$ signal at 500 ps delay and 60 min recording time are shown in Fig. 3(a) together with a measurement obtained at BESSY II [62] for comparison. The concentration and flatjet parameters are the same for both experiments. The synchrotron data was acquired in 8 min with a fluence of 270 mJ/cm^2, 150 ps delay, and 343 nm optical excitation. With both wavelengths, the same transient state is probed.

Extensive work has been published to understand the static and transient NEXAFS signal [63–67]. In summary, the optical excitation of the low spin ground state of the $[Fe(bpy)_3]^{2+}$ sample leads to a singlet metal-to-ligand charge-transfer (^{1}MLCT) state, which rapidly decays to a long-lived metal-centered (^{5}MC) high-spin quintet state. In the relaxation pathway to the ^{5}MC state, a sequential transition involving an intermediate ^{3}MC triplet state is likely involved. However, the direct transition from the MLCT to the ^{5}MC state is also discussed in the literature [68]. With our time resolution of 500 ps we exclusively probe the long-lived quintet state. This meta-stable state leads to an N-cage opening of 0.2 Å, which is reproduced by theory [69] and experiments [70]. The opening causes the observed energy shift of 0.3 eV between the ground and the excited state and an intensity change in the main absorption line.

The experimental difference spectrum is compared to the TD-DFT calculations in Fig. 3(b). The theoretical spectra are obtained by taking the difference between the calculated quintet or triplet ground state spectrum and the singlet ground state. The first two features around 399 eV are well reproduced by the triplet and quintet state. There is less agreement between the experiment and theory for the weaker features at 400.1 and 400.8 eV for the energy position and ΔA. For higher energies, the electrons are excited into unbound states where the particle-hole spectrum of the DFT calculations no longer correctly approximates the many-particle spectrum. Overall, the difference between the calculated quintet and triplet states is small. As a result, NEXAFS spectroscopy at the N K-edge is not a sensitive method to distinguish between the two states and cannot help to understand the ultrafast relaxation pathway.

Figure 3(c) shows the experimental error in the transient N K-edge spectrum, which follows the photon-counting statistics down

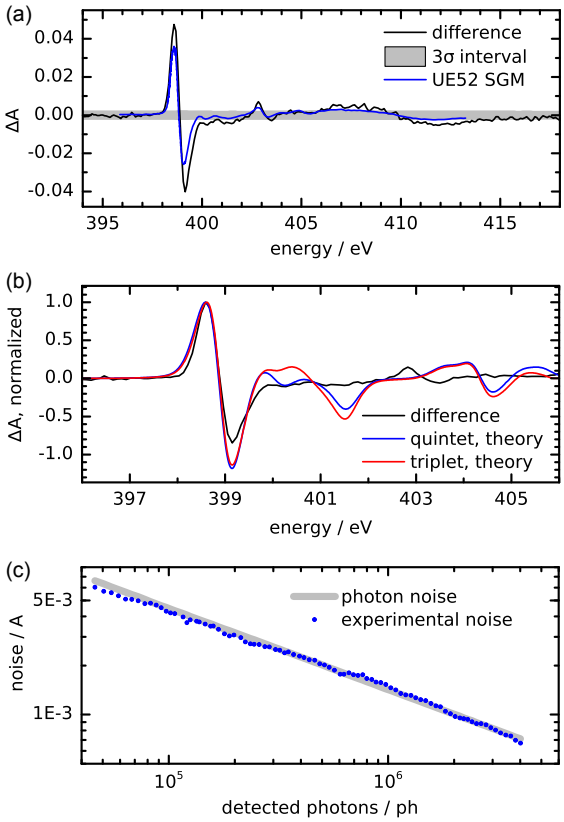

Fig. 3. (a) Transient signal of $[Fe(bpy)_3]^{2+}$ at the N K absorption edge excited with 120 mJ/cm^2 compared with synchrotron data. In gray the 3σ interval of the photon shot noise. (b) Comparison between the experimental difference signal in black with the theoretical difference spectrum of the triplet (red) and quintet (blue) state. (c) Progression of the experimental noise compared to the photon shot noise. The standard deviation in the pre-edge region of the experimental difference signal (362–395 eV) is defined as the experimental noise.

to at least $7\times10^{-4}A$. Since the photon noise is the lowest noise threshold in NEXAFS experiments, this result shows that neither the spectrometer nor instabilities of the flatjet [47] negatively affect the measurements.

In contrast to static and transient N K-edge NEXAFS spectra in the liquid phase, time-resolved C K-edge NEXAFS spectra for $[Fe(bpy)_3]^{2+}$ are missing in the literature. So far only static data for $[Fe(bpy)_3]^{2+}$ in the solid phase [71] and liquid phase [62] have been published. Furthermore, no theoretical assignment of the spectral features exists.

Measurements at the carbon K-edge are often challenging due to surface contaminations on the optics, which strongly absorb the incident radiation and imprint an absorption structure that can cause artifacts in the NEXAFS spectrum. Even a minor misalignment between the sample and the reference spectrum causes large artifacts in the NEXAFS spectrum [72] (S6). For our setup, alignment is guaranteed because of the simultaneous detection of reference and sample spectrum with the same RZP structure.

To better understand the NEXAFS spectrum measured at the C K-edge, TD-DFT calculations were performed. The experimental ground state spectrum, acquired in 44 min and the calculated spectrum, is shown in Fig. 4(a). The NEXAFS spectrum at the C K-edge shows two main absorption features at 284.4 eV and 285.3 eV originating from the transition of the C 1s into the π^* molecular orbital. The energy splitting is not due to different final states but is caused by a chemical shift of the C 1s orbitals, which depends on their position relative to the nitrogen atom inside the ring. The contribution of the different carbon atoms inside a single 2,2'-bipyridine ligand is shown in Fig. 4(b). Feature 1 originates from the ortho atoms a and b. The carbon atoms c and d form feature 2. Transitions from carbon atom e are in between features 1 and 2. The result is a partial selectivity of the carbon atoms inside the bipyridine ligands. The three bipyridine ligands contribute almost equally to the NEXAFS spectrum with C 1s energy differences below 10 meV. As in the case of the N K-edge results, the TD-DFT calculations for higher energies are unreliable. Therefore, we limit the energy range for the following discussion to the first two absorption features between 283 eV and 286.3 eV.

To theoretically describe the transient signal at 500 ps time delay, we adopt the widely accepted assumption that the optically excited $[Fe(bpy)_3]^{2+}$ is in the quintet ground state. The transient signal thus results from the difference between the singlet ground state and the quintet ground state. The broadened TD-DFT and difference spectra are shown in Fig. 4(c). The difference signal for the quintet state is largely caused by decreased absorption in the two main absorption features and increased absorption between these two. A slight broadening of the quintet state to the higher energy side leads to the feature at 285.8 eV. Compared to the large structural change around the Fe center, the geometry of the bipyridine ligand is almost unchanged in the quintet state. Only the carbon atoms a and b experience a small bond length change in the range of 0.01 Å. The change in the average charge density by 0.008 at the carbon atoms inside the bipyridine ligand is also small.

The main change between the singlet and quintet states is observed for the highest occupied molecular orbitals (HOMOs) and the lowest unoccupied molecular orbitals (LUMOs). Whereas the HOMOs in the singlet state are dominantly metal-centered, the LUMOs consist mostly of C p-orbitals with small N and negligible Fe contribution. In contrast, the HOMOs in the quintet state have little iron character but the LUMOs have a significant Fe 3d character. Compared to the singlet state, the quintet state is an open shell system with the spin population mainly located at the Fe atom. As a result, transitions into the partially unoccupied Fe 3d orbitals are possible. Because the structural changes are mostly limited to the Fe and N sites, the difference signal at the C K-edge is mostly caused by these transitions. Figure 4(c) also shows the triplet state's theoretical ground state spectrum and the theoretical difference spectrum between the singlet and the triplet ground state. Although the differences between the triplet and quintet are small at the C K-edge, there is a significant difference at 285.3 eV, where the difference signal is negative for the quintet but zero for the triplet. This result indicates that C K-edge NEXAFS can distinguish the triplet and quintet states. Thus, ultrafast transient NEXAFS measurements at the C K-edge could help to resolve the relaxation pathway of $[Fe(bpy)_3]^{2+}$. The relatively high signal strength combined with an absorption edge energy below 300 eV makes this measurement ideal for HHG sources.

In Fig. 4(d), the theoretical quintet difference spectrum and the measured transient signal with an 87 min measurement time are shown with the 3σ interval in gray and the static NEXAFS spectrum from Fig. 4(a). The calculation and measurement match qualitatively. The lower SNR compared to the N K-edge measurement is because the excited state is metal-centered, with the nitrogen atoms as the nearest neighbors.

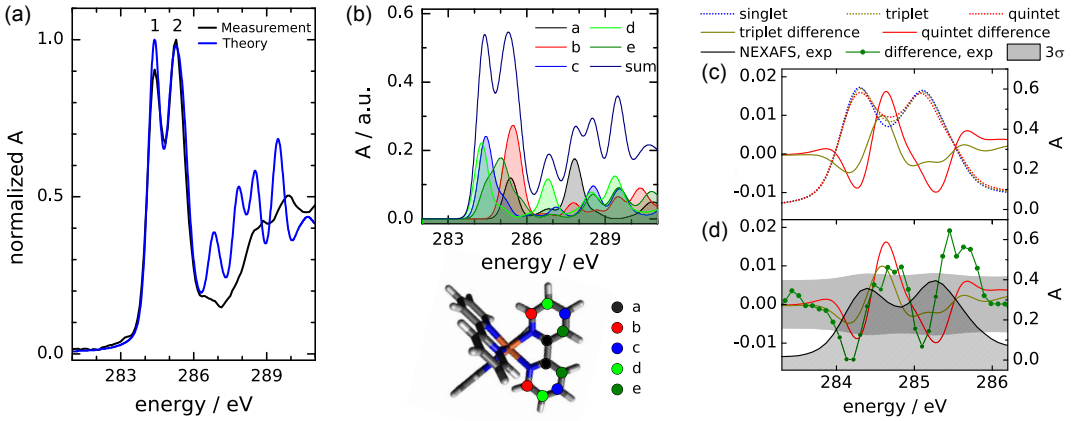

Fig. 4. (a) Measured static C K-edge spectrum of $[Fe(bpy)_3]^{2+}$ in black, calculated and broadened spectrum in blue. (b) Breakdown of the individual spectral contributions of the carbon atoms in a single bipyridine ligand caused by chemical shift of the C 1s orbitals. (c) Theoretical NEXAFS spectra for the singlet, triplet, and quintet configuration and the difference spectra for the triplet and quintet state. (d) Same theoretical difference spectra compared to the experimental difference spectrum at 500 ps time delay and the 3σ interval shown as a gray bar. In black, the measured ground state spectrum from graph (a).

4. PERFORMANCE AND EFFICIENCY CONSIDERATIONS

For the presented measurements, photon number estimations can be performed. The number of detected photons at the nitrogen K-edge is 3×10^4/s/0.1%BW, which matches well with the theoretically expected value of 6×10^4/s/0.1%BW given by the product of the peak spectral radiant intensity and the effective solid angle of the RZP, together with the transmission of the 2 µm water jet (0.64), the Ti-filter (0.67), the detector quantum efficiency (0.8), the height section on the flatjet used in the evaluation (0.67), and the data acquisition overhead (0.25). For the other edges, the number of detected photons is shown on the right side of Table 1 and the full spectra are shown in Section S8 in Supplement 1. Given that the spectrometer simultaneously measures the entire energy spectrum around an absorption edge, the integrated photon count within this range is a better indicator of the performance. For nitrogen K-edge NEXAFS with an energy range of 396–404 eV, this results in 6×10^5 detected photons per second.

A comparison between our LPP spectrometer, an optimized HHG setup at the Max-Born-Institut [5] and the synchrotron beamline UE52 SGM located at the radiation facility BESSY II [62,73] is shown in Table 2. Both the HHG and synchrotron setups are used for transient liquid phase experiments. The LPP setup detects two orders of magnitude more photons than the HHG setup in the energy range between 270 and 450 eV and allows measurements up to 1400 eV. The synchrotron end station, in turn, detects four to five orders of magnitude more photons than the LPP with a similar energy range and a higher energy resolving power of typically 4000. The advantage of the HHG source is the time resolution down to femtoseconds or even attoseconds. LPP sources for soft X-rays are limited to a few picosecond pulse durations, even with femtosecond driving lasers, due to the lifetime of the plasma region emitting the soft X-rays [74–76].

With the detected photon numbers of our LPP spectrometer and the absolute absorption values, it is possible to estimate the measurement time necessary to reach an SNR of 100 for different concentrations of $[Ni(CN)_4]^{2-}$ and $[Fe(bpy)_3]^{2+}$ in aqueous solution, as shown in Fig. 5. Based on the results of $[Fe(bpy)_3]^{2+}$, it is assumed that the noise is only limited by the photon counting

Table 2. Comparison between LPP Spectrometer, Optimized HHG Setup, and Synchrotron Beamline UE52 SGM[a]

	LPP	HHG	Synchrotron
Energy range/eV	210–1400	270–450	90–1500
Peak detected ph/s in transient measurement			
0.1% bandwidth	10^4	10^2	10^9
1% bandwidth	10^5	10^3	10^9
Time resolution/ps	500	0.03	50

[a]Because the energy is scanned in the synchrotron experiment, the amount of detected photons for 1% BW does not increase.

statistics, even for long measurement times. As a reasonable upper limit for the measurement time, one hour is marked as a black horizontal line in the graph. At that time, the minimum concentrations achievable are 5 mM for the C K-edge, 3 mM for the N K-edge, and 58 mM for the Ni L-edge. For increasing concentrations around 1000 mM the measurement time increases again for the C and N K-edges due to the sample absorption being above two. The higher concentrations required for the Ni L-edge measurements are due to the higher absorption of the solvent and the low absorption cross-section at the Ni L-edges. Details about the calculation are shown in Section S9 in Supplement 1.

To reach sub-millimolar concentrations, the efficiency of the current LPP setup needs to be improved. Multiple options exist, which can be implemented independently from each other. Figure 5 shows the effect for the Ni L-edge of $[Ni(CN)_4]^{2-}$. The dashed line is an easy-to-implement improvement with a more optimal mean thickness of the flatjet of 3 µm and a reduced source to the flatjet distance from 640 mm to 200 mm to better match the RZP viewing area to the flatjet area (factor 10). An RZP designed for a smaller source distance [78], and therefore a larger solid angle, could increase the efficiency by roughly a factor of 300. The dash–dot line shows the estimate for the optimized RZP and geometry. Finally, the use of an ultrafast CPA laser system with a higher average power and shorter pulse duration [79,80] could reduce the acquisition time by a factor of 50 and the time resolution of the LPP spectrometer to 10 ps [81]. The dotted line represents the estimate for a fully optimized setup based solely on existing,

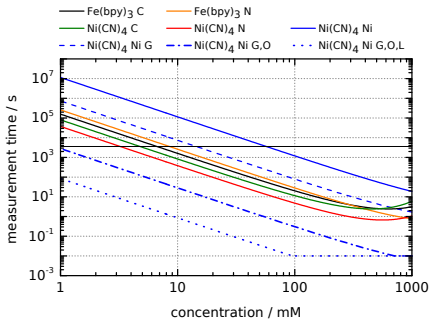

Fig. 5. Solid lines are the required measurement time to reach an SNR of 100 as a function of sample concentration at the C, N, and Ni absorption edges of $[Fe(bpy)_3]^{2+}$ and $[Ni(CN)_4]^{2-}$ with our current LPP setup. The expected reduction in measurement time due to improvements in geometry (G), RZP design (O), and laser upgrade (L) are shown in dashed lines. The minimum measurement time is set to 10 ms, which corresponds to the typical frame rate of 100 Hz for soft X-ray CMOS detectors [77]. The black bar indicates a measurement time of 60 min.

commercially available components. It offers up to five orders of magnitude more detected photons per second compared to the present setup, which would result in a measurement time of 1 min to reach an SNR of 100 at the Ni L-edge for a concentration of 1 mM. This demonstrates the remaining large potential of the LPP setup.

5. CONCLUSION

Combining advanced RZP optics with the broadband laser-produced plasma source enables static and time-resolved soft X-ray spectroscopy in the liquid phase in a spectral region between the water window and the L-edges of transition metals. The setup represents, to our knowledge, the only lab-based system that can measure the L-edges of all 3D metals in solution. The high spectral radiant intensity of the source and broadband detection results in an efficient setup where experiments with high concentrations can be performed in seconds or investigations of sample systems with low solubility, and therefore low concentrations, become possible. By using sample recycling, volumes down to 10 ml are achievable.

The common approach for NEXAFS spectroscopy is to use two separate measurements for the sample and reference spectrum, respectively. To measure both simultaneously shows clear advantages concerning noise and avoidance of artifacts in the spectra. Using the same optic and diffraction order results in a complete photon noise-limited setup down to at least $7 \times 10^{-4} A$. Because this detection scheme requires a large beam diameter in the sample plane, it is not easily transferable to most synchrotron radiation or HHG setups.

We present the NEXAFS spectra of all absorption edges of $[Ni(CN)_4]^{2-}$ in an aqueous solution. The static spectrum at the Ni L-edge showcases the ability to measure high energies. The results at the carbon edge demonstrate that lab-based systems can measure high-quality C K-edge spectra due to the low carbon contamination on their optics, which is often difficult at large-scale facilities.

The first time-resolved NEXAFS investigation at the C K-edge of the prototypical $[Fe(bpy)_3]^{2+}$ complex together with DFT calculations reveals that the transient signal is well reproduced with the model proposed in the literature to explain the nitrogen and iron edges, further strengthening the theoretical description. Additionally, transient measurements at the C K-edge have the potential to clarify further the ultrafast relaxation pathway of $[Fe(bpy)_3]^{2+}$.

In the future, an optimized geometry, optic and laser system can significantly improve the system's efficiency and time resolution. This would make it possible to measure sub-millimolar concentrations for a wide range of solvents and small sample volumes with a tabletop setup.

Funding. Horizon 2020 Framework Programme, Laserlab-Europe (871124); European Regional Development Fund (MOSFER 10168892).

Acknowledgment. We want to acknowledge Serena deBeer Max Planck Institute for Chemical Energy Conversion for the loan of the flatjet system and Renske van der Veen Helmholtz-Zentrum Berlin für Materialien und Energie for the provision of the $[Fe(bpy)_3]^{2+}$ sample. We thank Daniel Grötzsch Technische Universität Berlin for adapting the flatjet to the setup. H.S. would like to thank EFRE for funding.

Disclosures. The authors declare no conflicts of interest.

Data availability. Data underlying the results presented in this paper are not publicly available at this time but may be obtained from the authors upon reasonable request.

Supplemental document. See Supplement 1 for supporting content.

REFERENCES

1. G. Hahner, "Near edge X-ray absorption fine structure spectroscopy as a tool to probe electronic and structural properties of thin organic films and liquids," Chem. Soc. Rev. **35**, 1244–1255 (2006).
2. L. Royer, A. Bonnefont, T. Asset, *et al.*, "Cooperative redox transitions drive electrocatalysis of the oxygen evolution reaction on cobalt-iron core-shell nanoparticles," ACS Catal. **13**, 280–286 (2023).
3. M. Nagasaka and N. Kosugi, "Soft X-ray absorption spectroscopy for observing element-specific intermolecular interaction in solution chemistry," Chem. Lett. **50**, 956–964 (2021).
4. L. Schmermund, V. Jurkaš, F. F. Özgen, *et al.*, "Photo-biocatalysis: biotransformations in the presence of light," ACS Catal. **9**, 4115–4144 (2019).
5. C. Kleine, M. Ekimova, M.-O. Winghart, *et al.*, "Highly efficient soft x-ray spectrometer for transient absorption spectroscopy with broadband table-top high harmonic sources," Struct. Dyn. **8**, 034302 (2021).
6. A. D. Smith, T. Balciunas, Y. P. Chang, *et al.*, "Femtosecond soft-X-ray absorption spectroscopy of liquids with a water-window high-harmonic source," J. Phys. Chem. Lett. **11**, 1981–1988 (2020).
7. P.-A. Chevreuil, F. Brunner, U. Thumm, *et al.*, "Breakdown of the single-collision condition for soft x-ray high harmonic generation in noble gases," Optica **9**, 1448–1457 (2022).
8. P.-A. Chevreuil, F. Brunner, S. Hrisafov, *et al.*, "Water-window high harmonic generation with 0.8-μm and 2.2-μm OPCPAs at 100 kHz," Opt. Express **29**, 32996–33008 (2021).
9. T. Feng, A. Heilmann, M. Bock, *et al.*, "27W 2.1 μm OPCPA system for coherent soft X-ray generation operating at 10 kHz," Opt. Express **28**, 8724–8733 (2020).
10. C. Schmidt, Y. Pertot, T. Balciunas, *et al.*, "High-order harmonic source spanning up to the oxygen K-edge based on filamentation pulse compression," Opt. Express **26**, 11834–11842 (2018).
11. D. Garratt, M. Matthews, and J. Marangos, "Toward ultrafast soft x-ray spectroscopy of organic photovoltaic devices," Struct. Dyn. **11**, 010901 (2024).
12. H. Stiel, J. Braenzel, J. Tuemmler, *et al.*, "Ultrafast NEXAFS spectroscopy in the lab using laser-based sources and advanced X-ray optics," Proc. SPIE **11886**, 1188612 (2021).
13. M. Nagasaka, T. Hatsui, T. Horigome, *et al.*, "Development of a liquid flow cell to measure soft X-ray absorption in transmission mode: a test for liquid water," J. Electron Spectrosc. Relat. Phenom. **177**, 130–134 (2010).
14. M. Nagasaka, H. Yuzawa, and N. Kosugi, "Development and application of in situ/operando soft X-ray transmission cells to aqueous solutions and catalytic and electrochemical reactions," J. Electron Spectrosc. Relat. Phenom. **200**, 293–310 (2015).

15. M. Schellenberger, R. Golnak, W. Quevedo Garzon, *et al.*, "Accessing the solid electrolyte interphase on silicon anodes for lithium-ion batteries *in-situ* through transmission soft X-ray absorption spectroscopy," Mater. Today Adv. **14**, 100215 (2022).
16. S. Schreck, G. Gavrila, C. Weniger, *et al.*, "A sample holder for soft x-ray absorption spectroscopy of liquids in transmission mode," Rev. Sci. Instrum. **82**, 103101 (2011).
17. J. Meibohm, S. Schreck, and P. Wernet, "Temperature dependent soft x-ray absorption spectroscopy of liquids," Rev. Sci. Instrum. **85**, 103102 (2014).
18. I. Waluyo, C. Huang, D. Nordlund, *et al.*, "Increased fraction of low-density structures in aqueous solutions of fluoride," J. Chem. Phys. **134**, 224507 (2011).
19. M. L. Cowan, B. D. Bruner, N. Huse, *et al.*, "Ultrafast memory loss and energy redistribution in the hydrogen bond network of liquid H_2O," Nature **434**, 199–202 (2005).
20. D. Kraemer, M. L. Cowan, A. Paarmann, *et al.*, "Temperature dependence of the two-dimensional infrared spectrum of liquid H_2O," Proc. Natl. Acad. Sci. USA **105**, 437–442 (2008).
21. N. Huse, H. Wen, D. Nordlund, *et al.*, "Probing the hydrogen-bond network of water *via* time-resolved soft X-ray spectroscopy," Phys. Chem. Chem. Phys. **11**, 3951–3957 (2009).
22. N. Huse, T. K. Kim, L. Jamula, *et al.*, "Photo-induced spin-state conversion in solvated transition metal complexes probed via time-resolved soft X-ray spectroscopy," J. Am. Chem. Soc. **132**, 6809–6816 (2010).
23. H. Stollberg, M. Pokorny, and H. M. Hertz, "A vacuum-compatible wet-specimen chamber for compact X-ray microscopy," J. Microsc. **226**, 71–73 (2007).
24. C. Gosse, S. Stanescu, J. Frederick, *et al.*, "A pressure-actuated flow cell for soft X-ray spectromicroscopy in liquid media," Lab Chip **20**, 3213–3229 (2020).
25. G. Taylor, "Formation of thin flat sheets of water," Proc. R. Soc. London A **259**, 1–17 (1960).
26. J. C. T. Barnard, J. P. Lee, O. Alexander, *et al.*, "Delivery of stable ultra-thin liquid sheets in vacuum for biochemical spectroscopy," Front. Mol. Biosci. **9**, 1044610 (2022).
27. G. Galinis, J. Strucka, J. C. T. Barnard, *et al.*, "Micrometer-thickness liquid sheet jets flowing in vacuum," Rev. Sci. Instrum. **88**, 083117 (2017).
28. B. Ha, D. P. DePonte, and J. G. Santiago, "Device design and flow scaling for liquid sheet jets," Phys. Rev. Fluids **3**, 114202 (2018).
29. J. D. Koralek, J. B. Kim, P. Brůža, *et al.*, "Generation and characterization of ultrathin free-flowing liquid sheets," Nat. Commun. **9**, 1353 (2018).
30. D. J. Hoffman, H. A. Bechtel, D. A. Huyke, *et al.*, "Liquid heterostructures: generation of liquid-liquid interfaces in free-flowing liquid sheets," Langmuir **38**, 12822–12832 (2022).
31. C. J. Crissman, M. Mo, Z. Chen, *et al.*, "Sub-micron thick liquid sheets produced by isotropically etched glass nozzles," Lab Chip **22**, 1365–1373 (2022).
32. M. Ekimova, W. Quevedo, M. Faubel, *et al.*, "A liquid flatjet system for solution phase soft-x-ray spectroscopy," Struct. Dyn. **2**, 054301 (2015).
33. T. Lee, Y. Jiang, C. Rose-Petruck, *et al.*, "Ultrafast tabletop laser-pump–x-ray probe measurement of solvated $Fe(CN)_6^{4-}$," J. Chem. Phys. **122**, 084506 (2005).
34. T. E. Westre, P. Kennepohl, J. G. DeWitt, *et al.*, "A multiplet analysis of Fe K-edge 1s $\rightarrow$3d pre-edge features of iron complexes," J. Am. Chem. Soc. **119**, 6297–6314 (1997).
35. S. Iuchi and N. Koga, "Ultrafast electronic relaxation in aqueous $[Fe(bpy)_3]^{2+}$: a surface hopping study," J. Phys. Chem. Lett. **14**, 4225–4232 (2023).
36. I. Mantouvalou, K. Witte, D. Grötzsch, *et al.*, "High average power, highly brilliant laser-produced plasma source for soft X-ray spectroscopy," Rev. Sci. Instrum. **86**, 035116 (2015).
37. A. Jonas, H. Stiel, L. Glöggler, *et al.*, "Towards Poisson noise limited optical pump soft X-ray probe NEXAFS spectroscopy using a laser-produced plasma source," Opt. Express **27**, 36524–36537 (2019).
38. A. Jonas, K. Dammer, H. Stiel, *et al.*, "Transient sub-nanosecond soft X-ray NEXAFS spectroscopy on organic thin films," Anal. Chem. **92**, 15611–15615 (2020).
39. I. Mantouvalou, K. Witte, W. Martyanov, *et al.*, "Single shot near edge x-ray absorption fine structure spectroscopy in the laboratory," Appl. Phys. Lett. **108**, 201106 (2016).
40. J. W. M. Bush and A. E. Hasha, "On the collision of laminar jets: fluid chains and fishbones," J. Fluid Mech. **511**, 285–310 (2004).
41. Y.-P. Chang, Z. Yin, T. Balciunas, *et al.*, "Temperature measurements of liquid flat jets in vacuum," Struct. Dyn. **9**, 014901 (2022).
42. T. Buttersack, H. Haak, H. Bluhm, *et al.*, "Imaging temperature and thickness of thin planar liquid water jets in vacuum," Struct. Dyn. **10**, 034901 (2023).
43. S. Menzi, G. Knopp, A. Al Haddad, *et al.*, "Generation and simple characterization of flat, liquid jets," Rev. Sci. Instrum. **91**, 105109 (2020).
44. M. Ekimova, C. Kleine, J. Ludwig, *et al.*, "From local covalent bonding to extended electric field interactions in proton hydration," Angew. Chem. Int. Ed. **61**, e202211066 (2022).
45. H. Stiel, J. Braenzel, A. Jonas, *et al.*, "Towards understanding excited-state properties of organic molecules using time-resolved soft X-ray absorption spectroscopy," Int. J. Mol. Sci. **22**, 13463 (2021).
46. J. Probst, C. Braig, and A. Erko, "Flat field soft X-ray spectrometry with reflection zone plates on a curved substrate," Appl. Sci. **10**, 7210 (2020).
47. R. Y. Engel, M. Ekimova, P. S. Miedema, *et al.*, "Shot noise limited soft x-ray absorption spectroscopy in solution at a SASE-FEL using a transmission grating beam splitter," Struct. Dyn. **8**, 014303 (2021).
48. T. Katayama, Y. Inubushi, Y. Obara, *et al.*, "Femtosecond X-ray absorption spectroscopy with hard X-ray free electron laser," Appl. Phys. Lett. **103**, 131105 (2013).
49. T. Katayama, S. Owada, T. Togashi, *et al.*, "A beam branching method for timing and spectral characterization of hard X-ray free-electron lasers," Struct. Dyn. **3**, 034301 (2016).
50. G. Brenner, S. Dziarzhytski, P. S. Miedema, *et al.*, "Normalized single-shot X-ray absorption spectroscopy at a free-electron laser," Opt. Lett. **44**, 2157–2160 (2019).
51. R. Y. Engel, P. S. Miedema, D. Turenne, *et al.*, "Parallel broadband femtosecond reflection spectroscopy at a soft X-ray free-electron laser," Appl. Sci. **10**, 6947 (2020).
52. L. Le Guyader, A. Eschenlohr, M. Beye, *et al.*, "Photon-shot-noise-limited transient absorption soft X-ray spectroscopy at the European XFEL," J. Synchrotron. Radiat. **30**, 284–300 (2023).
53. C. Kolczewski, R. Püttner, O. Plashkevych, *et al.*, "Detailed study of pyridine at the C1s and N1s ionization thresholds: the influence of the vibrational fine structure," J. Chem. Phys. **115**, 6426–6437 (2001).
54. V. Vaz da Cruz, E. J. Mascarenhas, R. Büchner, *et al.*, "Metal–water covalency in the photo-aquated ferrocyanide complex as seen by multi-edge picosecond X-ray absorption," Phys. Chem. Chem. Phys. **24**, 27819–27826 (2022).
55. R. M. Jay, S. Eckert, R. Mitzner, *et al.*, "Quantitative evaluation of transient valence orbital occupations in a 3D transition metal complex as seen from the metal and ligand perspective," Chem. Phys. Lett. **754**, 137681 (2020).
56. R. M. Jay, S. Eckert, M. Fondell, *et al.*, "The nature of frontier orbitals under systematic ligand exchange in (pseudo-)octahedral Fe(II) complexes," Phys. Chem. Chem. Phys. **20**, 27745–27751 (2018).
57. K. Kunnus, W. Zhang, M. G. Delcey, *et al.*, "Viewing the valence electronic structure of ferric and ferrous hexacyanide in solution from the Fe and cyanide perspectives," J. Phys. Chem. B **120**, 7182–7194 (2016).
58. T. Hatsui and N. Kosugi, "Metal-to-ligand charge transfer in polarized metal L-edge X-ray absorption of Ni and Cu complexes," J. Electron Spectrosc. Relat. Phenom. **136**, 67–75 (2004).
59. T. Hatsui, Y. Takata, and N. Kosugi, "Strong metal-to-ligand charge transfer bands in Ni 2p photoabsorption of $K_2Ni(CN)_4 \cdot H_2O$," Chem. Phys. Lett. **284**, 320–324 (1998).
60. T. J. Penfold, M. Reinhard, M. H. Rittmann-Frank, *et al.*, "X-ray spectroscopic study of solvent effects on the ferrous and ferric hexacyanide anions," J. Phys. Chem. A **118**, 9411–9418 (2014).
61. R. M. Jay, V. Vaz da Cruz, S. Eckert, *et al.*, "Probing solute-solvent interactions of transition metal complexes using L-edge absorption spectroscopy," J. Phys. Chem. B **124**, 5636–5645 (2020).
62. M. Fondell, S. Eckert, R. M. Jay, *et al.*, "Time-resolved soft X-ray absorption spectroscopy in transmission mode on liquids at MHz repetition rates," Struct. Dyn. **4**, 054902 (2017).
63. K. Hong, H. Cho, R. W. Schoenlein, *et al.*, "Element-specific characterization of transient electronic structure of solvated Fe(II) complexes with time-resolved soft X-ray absorption spectroscopy," Acc. Chem. Res. **48**, 2957–2966 (2015).
64. A. Moguilevski, M. Wilke, G. Grell, *et al.*, "Ultrafast spin crossover in $[FeII(bpy)_3]^{2+}$: revealing two competing mechanisms by extreme ultraviolet photoemission spectroscopy," ChemPhysChem **18**, 465–469 (2017).

65. W. Gawelda, A. Cannizzo, V.-T. Pham, *et al.*, "Ultrafast nonadiabatic dynamics of $[FeII(bpy)_3]^{2+}$ in solution," J. Am. Chem. Soc. **129**, 8199–8206 (2007).
66. S. Iuchi and N. Koga, "A model electronic Hamiltonian to describe low-lying d-d and metal-to-ligand charge-transfer excited states of $[Fe(bpy)_3]^{2+}$," J. Comput. Chem. **42**, 166–179 (2021).
67. H. Cho, M. L. Strader, K. Hong, *et al.*, "Ligand-field symmetry effects in Fe(II) polypyridyl compounds probed by transient X-ray absorption spectroscopy," Faraday Discuss. **157**, 463–474 (2012).
68. G. Auböck and M. Chergui, "Sub-50-fs photoinduced spin crossover in $[Fe(bpy)_3]^{2+}$," Nat. Chem. **7**, 629–633 (2015).
69. B. E. Van Kuiken, H. Cho, K. Hong, *et al.*, "Time-resolved X-ray spectroscopy in the water window: elucidating transient valence charge distributions in an aqueous Fe(II) complex," J. Phys. Chem. Lett. **7**, 465–470 (2016).
70. W. Gawelda, V.-T. Pham, M. Benfatto, *et al.*, "Structural determination of a short-lived excited iron(II) complex by picosecond X-ray absorption spectroscopy," Phys. Rev. Lett. **98**, 057401 (2007).
71. P. S. Johnson, P. L. Cook, I. Zegkinoglou, *et al.*, "Electronic structure of Fe- vs. Ru-based dye molecules," J. Chem. Phys. **138**, 044709 (2013).
72. I. Mantouvalou, A. Jonas, K. Witte, *et al.*, "Optimizing soft X-ray NEXAFS spectroscopy in the laboratory," Proc. SPIE **10243**, 1024308 (2017).
73. F. Senf, F. Eggenstein, U. Flechsig, *et al.*, "Performance of the first undulator beamline U49-1-SGM at BESSY II," Nucl. Instrum. Methods Phys. Res. A **467-468**, 474–478 (2001).
74. M. M. Murnane, H. C. Kapteyn, and R. W. Falcone, "High-density plasmas produced by ultrafast laser pulses," Phys. Rev. Lett. **62**, 155–158 (1989).
75. M. M. Murnane, H. C. Kapteyn, M. D. Rosen, *et al.*, "Ultrafast X-ray pulses from laser-produced plasmas," Science **251**, 531–536 (1991).
76. D. Giulietti and L. A. Gizzi, "X-ray emission from laser-produced plasmas," Riv. Nuovo Cimento **21**, 1–93 (1998).
77. A. Jonas, S. Staeck, B. Kanngießer, *et al.*, "Laboratory quick near edge x-ray absorption fine structure spectroscopy in the soft x-ray range with 100 Hz frame rate using CMOS technology," Rev. Sci. Instrum. **92**, 023102 (2021).
78. Z. Yin, J. Rehanek, H. Löchel, *et al.*, "Highly efficient soft X-ray spectrometer based on a reflection zone plate for resonant inelastic X-ray scattering measurements," Opt. Express **25**, 10984–10996 (2017).
79. S. Rajhans, E. Escoto, N. Khodakovskiy, *et al.*, "Post-compression of multi-millijoule picosecond pulses to few-cycles approaching the terawatt regime," Opt. Lett. **48**, 4753–4756 (2023).
80. A.-L. Viotti, S. Alisauskas, M. Seidel, *et al.*, "FLASH free electron laser pump-probe laser concept based on spectral broadening of high-power ytterbium picosecond systems in multi-pass cells," Rev. Sci. Instrum. **94**, 023002 (2023).
81. D. Schick, M. Borchert, J. Braenzel, *et al.*, "Laser-driven resonant magnetic soft-X-ray scattering for probing ultrafast antiferromagnetic and structural dynamics," Optica **8**, 1237–1242 (2021).